The Imprint of Strong-Storm Tracks on Winter Weather in North America

KATHERINE E. LUKENS

Department of Atmospheric and Oceanic Science, and Cooperative Institute for Climate and Satellites–Maryland, Earth System Science Interdisciplinary Center, University of Maryland, College Park, College Park, Maryland

ERNESTO HUGO BERBERY

Cooperative Institute for Climate and Satellites–Maryland, Earth System Science Interdisciplinary Center, University of Maryland, College Park, College Park, Maryland

KEVIN I. HODGES

Department of Meteorology, University of Reading, Reading, United Kingdom

(Manuscript received 22 June 2017, in final form 27 November 2017)

ABSTRACT

Northern Hemisphere winter storm tracks and their relation to winter weather are investigated using NCEP CFSR data. Storm tracks are described by isentropic PV maxima within a Lagrangian framework; these correspond well with those described in previous studies. The current diagnostics focus on strong-storm tracks, which comprise storms that achieve a maximum PV exceeding the mean value by one standard deviation. Large increases in diabatic heating related to deep convection occur where the storm tracks are most intense. The cyclogenesis pattern shows that strong storms generally develop on the upstream sectors of the tracks. Intensification happens toward the eastern North Pacific and all across the North Atlantic Ocean, where enhanced storm-track-related weather is found. In this study, the relation of storm tracks to near-surface winds and precipitation is evaluated. The largest increases in storm-track-related winds are found where strong storms tend to develop and intensify, while storm precipitation is enhanced in areas where the storm tracks have their highest intensity. Strong storms represent about 16% of all storms but contribute 30%–50% of the storm precipitation in the storm-track regions. Both strong-storm-related winds and precipitation are prone to cause storm-related losses in the eastern U.S. and North American coasts. Over the oceans, maritime operations are expected to be most vulnerable to damage offshore of the U.S. coasts. Despite making up a small fraction of all storms, the strong-storm tracks have a significant imprint on winter weather in North America potentially leading to structural and economic loss.

1. Introduction

Two well-documented midlatitude winter storm tracks in the Northern Hemisphere (NH) affect North American weather and climate: the Pacific storm track, which extends eastward across the North Pacific Ocean, and the Atlantic storm track, which extends northeastward across the North Atlantic Ocean. Elsewhere in the NH midlatitudes there is the Mediterranean storm track, which spans eastward across the Mediterranean Sea to the Middle East (Hoskins and Hodges 2002). The storm tracks are characterized as large narrow bands of high baroclinic instability along which individual storms tend to propagate, and are maintained by the continuous downstream development of baroclinic disturbances (Simmons and Hoskins 1979; Wallace et al. 1988; Orlanski and Chang 1993). The upper-tropospheric winds (i.e., the 200-hPa jet stream) and divergence aloft produce cyclonic circulation poleward of the zonal flow, enhancing cyclonic shear and generating upstream confluence that can predominantly maintain the mean baroclinicity needed for continued downstream eddy activity (Wallace et al. 1988; Hoskins and Valdes 1990). Even in cases of weak instability, the downstream radiation of kinetic energy in the form of ageostrophic geopotential fluxes contributes to the growth and intensification of new eddies at the expense of upstream decaying eddies (Simmons and Hoskins 1979; Orlanski and Chang 1993). Baroclinic disturbances propagate

Corresponding author: Ernesto Hugo Berbery, berbery@umd.edu

DOI: 10.1175/JCLI-D-17-0420.1

downstream as large-scale wave packets with a group velocity that primarily dictates the speed at which new eddies develop (Orlanski and Chang 1993).

Many factors influence the NH storm-track distribution, including sea surface temperature (SST) gradients, uneven heating, and orography (Hoskins and Valdes 1990; Held 1993; Brayshaw et al. 2008, 2009; Chang 2009). A strong midlatitude SST gradient alongside a reduced subtropical SST gradient will generally strengthen the storm tracks and shift them poleward (Brayshaw et al. 2008). In the North Atlantic the large SST gradient formed by the protrusion of the warm Gulf Stream into the cool higher-latitude ocean induces surface wind convergence on the warm side of the Gulf Stream front, intensifying the vertical wind velocity and vertical instability, in turn enhancing convection and storm development (Minobe et al. 2008, 2010).

Uneven diabatic heating induced in part by land–sea temperature contrasts plays a role in storm-track modulation (Hoskins and Valdes 1990; Chang 2009). As cool westerly flow off the land passes over warmer western oceans, the surface air warms rapidly, triggering the generation of surface sensible heat fluxes that act to destabilize the atmosphere (Mak 1998). The sensible heat fluxes counter the damping effect of poleward eddy heat fluxes, preserving baroclinicity at the surface and maintaining the storm tracks through the development of unstable waves aloft (Hotta and Nakamura 2011). Asymmetries in diabatic heating partly account for the greater strength of the Atlantic storm track compared to the Pacific storm track, despite the lower baroclinicity in the Atlantic (Chang 2009). For instance, the large land–sea temperature gradient in winter induced by strong airmass contrasts between cold air over northeastern North America and warmer air over the Gulf Stream form a region of particularly high baroclinic instability along an axis that follows the North American east coast (Brayshaw et al. 2009). Storms tend to deepen and intensify leeward of the Appalachian Mountains (Colucci 1976), and the baroclinic zone over the North American east coast promotes the further amplification of storms, including nor'easters (Davis and Dolan 1993). Additionally, the strength and areal width of marine storms are determined by the intensity of the diabatic heating (Mak 1998).

As for orographic influences, mountainous terrain mainly acts to suppress storm-track activity by blocking or deflecting the westerly flow over land (Chang 2009). The Rocky Mountains deflect westerly Pacific cyclones/storms southward, which leads to a southwest–northeast (SW–NE) tilt in the upper-tropospheric jet, the subsequent downstream flow, and the Atlantic storm track, dynamically separating the Northern Hemisphere storm tracks (Brayshaw et al. 2009; Chang 2009). The Atlantic track lies coincident with the SW–NE axis of the low-level baroclinic zone that follows the North American east coast, further enhancing cyclonic activity in the region of the Atlantic storm track (Brayshaw et al. 2009).

During winter, the Pacific and Atlantic storm tracks are collocated with climatological precipitation maxima that exceed 6 mm day^{-1} (Adler et al. 2003; Hawcroft et al. 2016; Xie et al. 2017). Extremely high precipitation is produced primarily by extratropical storms with the most heavily precipitating storms contributing substantially to the winter climatological precipitation (Maddox et al. 1979; Hawcroft et al. 2012; Pfahl and Wernli 2012). In general in the NH, over half of the mean total winter precipitation in the midlatitudes is associated with frontal systems and related cyclonic activity (Catto et al. 2012). Specifically in North America, over 70% of winter precipitation is associated with low-level cyclonic activity (Hawcroft et al. 2012). It has also been found that precipitation and upper-level zonal flow are highly correlated over the midlatitude oceans and over land upstream of high orography, supporting the notion that strong baroclinic cyclones aloft lead to large accumulations of precipitation at the surface (Maddox et al. 1979; Garreaud 2007; Pfahl and Wernli 2012). Accordingly, storm-track modulation can be associated with changes in the frequency of extreme precipitation and wind events, which can profoundly affect a region's climate (Chang et al. 2002; Ma and Chang 2017). This can happen if a northward shift and deepening of the semipermanent Aleutian low in the high latitudes of the North Pacific Ocean occurs as it can then draw the Pacific storm track poleward and subsequently amplify winter precipitation in northwestern North America (Salathé 2006).

Previous studies have used different variables and metrics to represent storm tracks, including mean sea level pressure (MSLP), geopotential height, and the meridional component of the upper-tropospheric wind (e.g., Gulev et al. 2001; Hoskins and Hodges 2002; Raible 2007). MSLP and 500-hPa geopotential height are dominated by large scales, making small-scale, high-frequency features like cyclones difficult to identify without bias toward larger, slower disturbances (Wallace et al. 1988; Hoskins and Hodges 2002). The upper-level meridional wind tends to better capture the higher frequencies and reveals downstream-developing wave trains along the storm tracks (Chang and Orlanski 1993; Berbery and Vera 1996). Low-level relative vorticity and isentropic potential vorticity (PV) are also useful to track storms because of their dependence on higher order derivatives that allows for the detection of small-scale features such as cyclogenesis and cyclolysis

(Hoskins and Hodges 2002). PV, in particular, is an ideal dynamical tracer because of its conservation properties in an adiabatic, frictionless flow (Holton 2004). In the Northern Hemisphere, a positive (cyclonic) PV anomaly, which generally corresponds to an upper-tropospheric pressure trough, induces a vortex with cyclonic circulation (Hoskins et al. 1985; Hoskins and Hodges 2002). Because PV considers both absolute vorticity and static stability, it encapsulates many of the dynamic and thermodynamic properties of the atmospheric circulation while also conforming to the principle of invertibility, which establishes that the three-dimensional wind and temperature fields are induced by the PV structure if relatively fast-moving waves are neglected (Hoskins et al. 1985; Hoskins 1997).

This study discusses the characteristics of the storm tracks as constituted by storms that achieve high potential vorticity and will thus be called ''strong-storm tracks.'' The primary objectives of the study address the following questions: 1) How do strong-storm tracks relate to surface weather and diabatic heating distributions? 2) What are the potential damaging effects of very high near-surface winds and precipitation rates associated with the strong-storm tracks that could lead to structural and economic loss in North America? We also discuss the robustness of the results by using an independent dataset of observed precipitation.

The structure of the article is as follows: section 2 describes the datasets and cyclone tracking method used. Section 3 discusses the properties of the strong-storm tracks that affect North America's winter weather, while section 4 examines the relation between the strong-storm tracks and the potential destructive effects of the associated wind and precipitation. Section 5 summarizes the key findings.

2. Data and methodology

a. Datasets

The National Centers for Environmental Prediction (NCEP) Climate Forecast System Reanalysis (CFSR; Saha et al. 2010a) product is the most recent complete compilation of global reanalysis data generated by NCEP. The CFSR couples the atmosphere, ocean, land surface, and sea ice to provide our best four-dimensional (4D) view of Earth's natural state, constrained by observations, every 6 h. The global atmospheric data have a horizontal grid spacing of 38 km, 64 vertical sigma–pressure levels, and are archived on a 0.5° × 0.5° latitude–longitude grid. The gridded statistical interpolation (GSI) scheme assimilates atmospheric variables including global precipitation rates derived from rain gauge and satellite observations into CFSR. The coupled assimilation provides a more complete and better-quality dataset of precipitation than past NCEP reanalyses that neglect coupling in the data assimilation, with better correspondence between the model physics and observed precipitation (Saha et al. 2010b; Wang et al. 2011). The accuracy of CFSR is improved over past NCEP reanalyses in part because of higher spatial and temporal resolutions, the assimilation of bias-corrected observations, and the coupling to sea ice and the ocean (Saha et al. 2010b). Despite the improvements in CFSR, an artificial discontinuity around October 1998 in the wind and precipitation time series has previously been found. The ingestion of satellite observations often marks the onset of artificial trends in other reanalysis datasets (Bengtsson et al. 2004), and CFSR is no different. The discontinuity in CFSR is thought to be due to the introduction of the assimilation of data from the low-Earth polar-orbiting Advanced Television and Infrared Observation Satellite (TIROS) Operational Vertical Sounder (ATOVS) satellite, which contributes to less spinup of the initial moisture, resulting in a more humid atmosphere after 1998 (Saha et al. 2010b; Chelliah et al. 2011; Wang et al. 2011; Zhang et al. 2012). Our study uses CFSR data for DJF from 1980 to 2010 and examines this discontinuity to assess the potential effects on our results.

The Global Precipitation Climatology Project (GPCP) 1° daily dataset (Huffman et al. 2012) of precipitation accumulations centered on 1200 UTC is used to complement the reanalysis information. Since October 1996, the GPCP has provided high-quality, high-resolution global precipitation data. The daily dataset is derived from the GPCP Monthly Precipitation Analysis, version 2, by combining in situ data (i.e., surface rain gauges) with histograms of 3-hourly infrared brightness temperatures from geosynchronous-orbit satellite infrared data and precipitation derived from atmospheric parameters retrieved from low Earth orbit satellites (Huffman et al. 2001; Adler et al. 2003; Pendergrass et al. 2015). In this study, GPCP daily precipitation is used for DJF from 1999 to 2010 and is taken as ''ground truth'' although some estimates, particularly over oceans, may be less reliable (Adler et al. 2012).

b. Tracking of storms

Small-scale isentropic potential vorticity maxima at the 320-K level (PV_{320}) at 6-hourly intervals are objectively tracked in DJF for 1980–2010 following the Lagrangian approach discussed in Hoskins and Hodges (2002). The method first identifies cyclones as PV_{320} anomalies that exceed 0.5 potential vorticity units (PVU; 1 PVU = $10^{-6}\,K\,kg^{-1}\,m^2\,s^{-1}$) on a NH polar stereographic projection, which helps to prevent

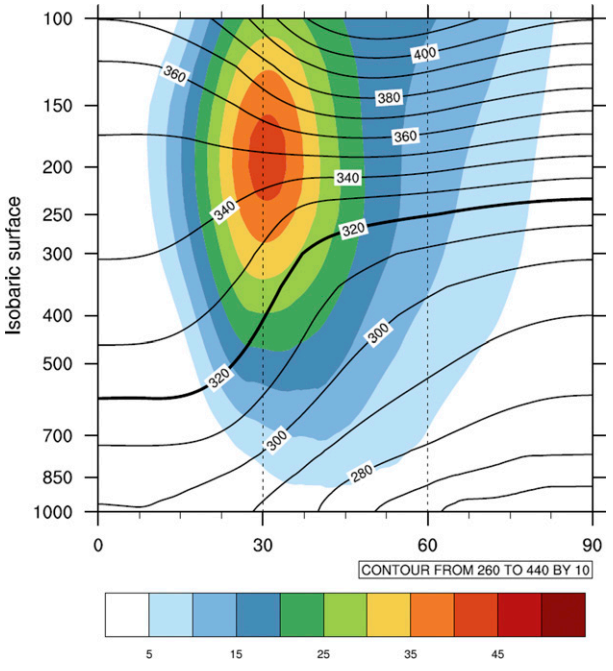

FIG. 1. DJF mean zonal state in the Northern Hemisphere for 1980–2010. The mean zonal wind is shaded with 5.0 m s^{-1} intervals. Line contours indicate the vertical distribution of mean zonal isentropic surfaces at a 10-K contour interval. The thick black line highlights the surface where $\theta = 320$ K on which the midlatitude storm tracks are defined.

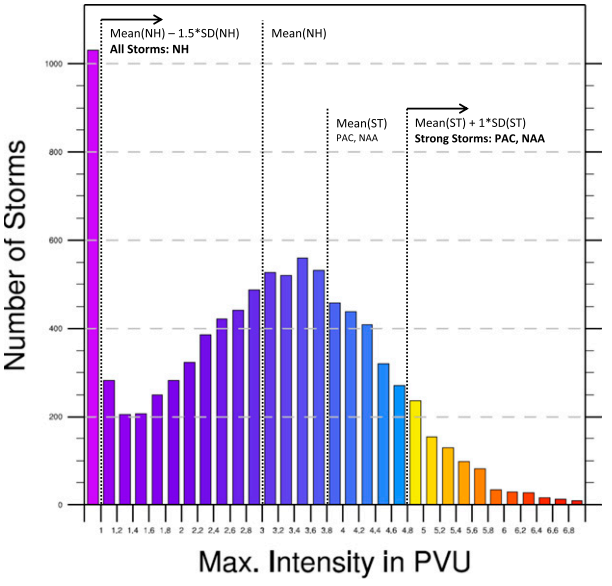

FIG. 2. Histogram of all DJF storms binned by maximum intensity in the Northern Hemisphere for 1980–2010. Maximum intensity bins are shown in the x direction at an interval of 0.2 PVU. Storms included in the all-storm-track analysis have maximum intensities of 1 PVU or greater. Strong storms that follow the Pacific (PAC) or NAA storm tracks have maximum intensities of 4.8 PVU or greater and are highlighted in warm colors. In parentheses in the labels, NH signifies the statistics for the Northern Hemisphere, whereas ST indicates the statistics for the PAC and NAA storm tracks.

latitudinal bias in the identification of cyclones at high latitudes (Sinclair 1997). The PV_{320} threshold of 0.5 PVU is significantly low to account for most possible storms: in this case about 296 cyclones per DJF season are identified that satisfy the posttracking filters (discussed below). The 320-K isentrope is chosen as the level of analysis as it resides in the mid-to-upper troposphere near the upper-level jet stream (Fig. 1) where Rossby wave–induced baroclinic instability tends to occur (Hoskins 1991). The PV_{320} anomalies are produced by applying a spherical harmonic analysis to the PV_{320} field and removing the background planetary-scale waves with total wavenumbers less than or equal to 5 and reducing the resolution to spectral T42 to reduce noise. Additionally, a spectral taper is applied to the spectral coefficients to further reduce noise (Hoskins and Hodges 2002). This has been found to be a conservative but useful approach when examining fields that are dominated by a large-scale background and are very noisy at high resolutions and focuses on the synoptic spatial scales of cyclones. The identified PV_{320} maxima are initially linked using a nearest-neighbor method to form tracks and are then refined using a constrained optimization approach, which swaps points between tracks to maximize the track smoothness (Hodges 1994, 1995). Constraints are applied adaptively for maximum propagation speed and track smoothness (Hodges 1999) suitably chosen for the extratropics.

Following completion of the tracking, a filter is applied to retain only those cyclones that last at least two days and travel farther than 1000 km. These conditions act as spatial and temporal filters to remove short duration or semistationary eddies. Considering that extratropical storms at 320 K in the NH have an average $PV_{max} = 3$ PVU and a standard deviation $(PV_{max})_{SD} = 1.3$ PVU, we define "all-storm tracks" as those shaped by storms with maximum PV that exceed a low threshold of $\overline{PV}_{max} - 1.5 \times (PV_{max})_{SD} \cong 1$ PVU. As apparent in Fig. 2, this threshold captures weak cyclogenesis and provides a large number of cases for the analysis: on average, about 259 storms per season that satisfy the posttracking filters that comprise the extratropical NH all-storm tracks.

Storms in the Pacific and Atlantic Oceans have an average PV_{max} of 3.8 PVU with a standard deviation of 1 PVU (both regions have the same values, despite being computed separately). Strong-storm tracks represent those storms in the Pacific and Atlantic Oceans with maximum PV that exceeds a higher threshold of $\overline{PV}_{max} + 1 \times (PV_{max})_{SD} = 3.8$ PVU + 1 PVU = 4.8 PVU as

TABLE 1. Statistics for the DJF strong-storm tracks for (top) the entire Northern Hemisphere, (middle) the Pacific storm track, and (bottom) the NAA storm track. In the Pacific and NAA storm-track data, only strong storms that develop within the specified storm-track domain are included. The first column shows the values for the entire 31-yr period. The following two columns denote the early and later periods. The last three columns highlight the values for each decade.

	1980–2010	1980–98	1999–2010	1981–90	1991–2000	2001–10
Northern Hemisphere						
No. of strong storms (season^{-1})	26	24	29	26	24	30
Mean intensity (PVU)	3.8	3.8	3.8	3.8	3.8	3.8
Avg max intensity (PVU)	5.4	5.4	5.4	5.4	5.4	5.4
Pacific storm track						
No. of strong storms (season^{-1})	9	9	9	10	7	9
Mean intensity (PVU)	3.8	3.8	3.8	3.8	3.7	3.8
Avg max intensity (PVU)	5.3	5.3	5.3	5.3	5.3	5.3
NAA storm track						
No. of strong storms (season^{-1})	6	5	8	5	6	8
Mean intensity (PVU)	3.8	3.8	3.8	3.8	3.8	3.9
Avg max intensity (PVU)	5.3	5.3	5.3	5.3	5.3	5.3

also noted in Fig. 2. Strong storms represent about 16% of all storms that develop in both regions and correspond to similar percentiles of the storm strength distribution in each basin. On average, nine (six) strong storms per season develop in the storm-track region over the Pacific (Atlantic) Ocean (Table 1).

The statistics of a large number of the cyclone trajectories describe the main properties of the Northern Hemisphere storm tracks, including the track density, genesis density, lysis density, and mean storm-track intensity. Following Hoskins and Hodges (2002), the track density statistic is calculated by using a single point from each track nearest to each estimation point for each PV cyclone trajectory; the genesis density statistic uses the first detected positions of the cyclones; likewise, the lysis density statistic uses the last detected positions of the cyclones, and the spherical kernel density estimator method (Hodges 1996, 2008). The genesis and lysis densities are computed as probability density functions (pdfs) and scaled to number densities (per unit area per month) by multiplying by the number of points and scaling to a unit area equivalent to a 5° spherical cap ($\sim 10^6$ km^2); in the case of the track density, the raw statistic is not a pdf but is scaled to number density by multiplying by the number of tracks and scaled to a unit area equivalent to a 5° spherical cap. The mean intensity statistic is calculated using a kernel regression estimator (Hodges 1996) applied to the PV intensity for all points along the cyclone trajectories. For both the density and regression estimators adaptive smoothing is used (Hodges 1996).

Sensitivity tests were carried out to assess the robustness of the results in relation to (i) the isentropic level of the analysis on which to describe the storm tracks and (ii) the PV intensity threshold, used for the initial identification, above which to consider a cyclone (not shown). An analysis of storm tracks on different isentropic surfaces (not shown) resulted in the choice of the 320-K isentrope as it is a good intermediate level on which the storm-track features are best represented. The structures and relative intensities of the storm tracks exhibit a lack of sensitivity to the PV intensity threshold (not shown).

In general, the storm tracks and the diabatic heating in the corresponding regions act symbiotically in that the presence of the heating helps to maintain the baroclinicity needed for cyclone activity, which in turn influences the three-dimensional diabatic heating distribution (Hoskins and Valdes 1990). With this codependence between the storm tracks and diabatic heating in mind, our study explores the direct relationship between the heating and the storm tracks that influence North America's weather. The diabatic heating is computed diagnostically at each level between 900 and 100 hPa as the residual in the thermodynamic equation (e.g., Hoskins et al. 1989; Barlow et al. 1998; Holton 2004):

$$\frac{\dot{Q}(x,y,p,t)}{c_p} = \frac{\partial T}{\partial t} + \mathbf{v}\cdot\nabla T + \omega\left(\frac{\partial T}{\partial p} - \frac{RT}{c_p p}\right), \quad (1)$$

where $\dot{Q}/c_p$ is the residual heating (K day^{-1}), T is the temperature, $\mathbf{v}$ is the horizontal wind vector, ω is the vertical wind in pressure coordinates, R is the gas constant for dry air, c_p is the specific heat for dry air at constant pressure, and p is the pressure level. The residual is then vertically averaged to yield daily diabatic heating estimates of the free atmosphere.

To establish the relationship between the storm tracks and diabatic heating, near-surface winds, and precipitation, we follow a similar approach to that discussed in Hawcroft et al. (2012) and related literature. Each

variable is considered to be associated with a cyclone if it is found within a particular circular area around the cyclone center. Precipitation from both reanalysis and observations is considered to be associated with a storm if it is found within a 12° circular area around each storm center, as this is a typical storm precipitation footprint size in the Northern Hemisphere winter (Hawcroft et al. 2012). The reanalysis precipitation is associated with storm centers identified at corresponding 6-hourly time steps, while the GPCP observations are associated with storm center positions at 1200 UTC each day. Other variables have been reported to be greatly affected within the core of a cyclone represented by a 5° cyclone radius (Hawcroft et al. 2012, 2016), and this is the choice we consider for diabatic heating and near-surface winds that are associated with the storm centers every 6 h. The storm-related heating, winds, and precipitation fields in the figures are masked out at grid points where the average number of storms is below some very low number (in this case 0.5 storms per unit area per month) in order to highlight the midlatitude main activity storm-track regions.

c. Storm loss metrics

To examine the relation between strong-storm tracks and high wind speeds that could lead to potential damage at the surface, we employ a metric defined by Klawa and Ulbrich (2003). The metric is represented by a loss index that highlights areas where strong storms are likely to produce considerable damage by way of winds that exceed the local 98th percentile. Following Klawa and Ulbrich (2003),

$$\text{loss index} = \sum_{\text{seasons}} N_{\text{pop}} \left(\frac{v}{v_{98}} - 1 \right)^3 \quad \text{for} \quad v \geq v_{98}, \tag{2}$$

where N_{pop} is the local population number, v is the local wind speed related to the storm tracks, and v_{98} is the local wind speed at the 98th quantile for 1980–2010. Use of this metric has led to the successful reproduction of storm loss in Germany at the end of the twentieth century, in turn leading to a storm loss risk assessment for the nation in the twenty-first century (Klawa and Ulbrich 2003; Donat et al. 2011).

Precipitation and storm severity are inherently linked in part by condensational heating and the enhancement of moisture flux convergence (Trenberth et al. 2003). To our knowledge and unlike for winds, a general relationship between storm-track precipitation and damaging effects has not yet been established. We adopt a simple approach in which we assume that areas that are most likely to experience loss are those where the storm-track precipitation exceeds the local 98th percentile.

3. Dynamics of storm tracks

a. Environment

The Eady growth rate, used in this study, combines information of the static stability and the wind vertical shear for the 850–700-hPa layer and is frequently used as a measure of baroclinic instability (Lindzen and Farrell 1980). Following Hoskins and Valdes (1990), Fig. 3 shows that 1) regions of large baroclinic instability are found over the western Pacific and Atlantic Oceans (Fig. 3a), and 2) the largest region of low-level baroclinic instability lies poleward of the 200-hPa jet stream (Fig. 3b). Note that a region of high instability in the western Pacific is zonal in orientation and parallels the strong 200-hPa jet. In the western Atlantic, the region of lower-troposphere instability also parallels the local upper-level jet maximum with a SW–NE orientation that follows the eastern North American coastline. A secondary region of baroclinic instability is found in the southeast of the Mediterranean Sea and is also poleward of the corresponding local upper-level jet maximum.

b. Physical properties of the storm tracks

The characteristics of the 1980–2010 strong winter storm tracks (those with $\text{PV}_{\text{max}} \geq 4.8$ PVU) are depicted in Fig. 4. In Fig. 4a, the midlatitude trajectories of individual strong storms converge into quasi-zonal bands of high cyclonic activity that form the strong-storm tracks. The number of individual strong storms per unit area, or strong-storm-track density (Fig. 4b), is largest over the Pacific, North American–Atlantic (NAA), and Mediterranean regions. As expected, and in agreement with Wallace et al. (1988) and Hoskins and Valdes (1990), the three regions of strong-storm tracks are concentrated poleward of the upper-level jets where there is amplified cyclonic shear and enhanced downstream development of baroclinic disturbances (Figs. 3b and 4b). Figure 4b also highlights that the strong-storm-track density (shaded) resembles the track density for all winter storms (those with $\text{PV}_{\text{max}} \geq 1$ PVU, the threshold for all-storm tracks, contours), the latter of which is consistent with those presented in Hoskins and Hodges (2002) and other studies. This is particularly evident over the North Atlantic where the NAA storm tracks for both strong storms and all storms extend northeastward from central North America into the higher latitudes near Iceland. The mean intensity statistic denotes the average strength of the strong-storm tracks identified in DJF (Fig. 4c). The strong-storm tracks are most intense where the corresponding track densities are highest (i.e., in the eastern North Pacific and western North Atlantic Oceans, and the Mediterranean Sea). The Pacific

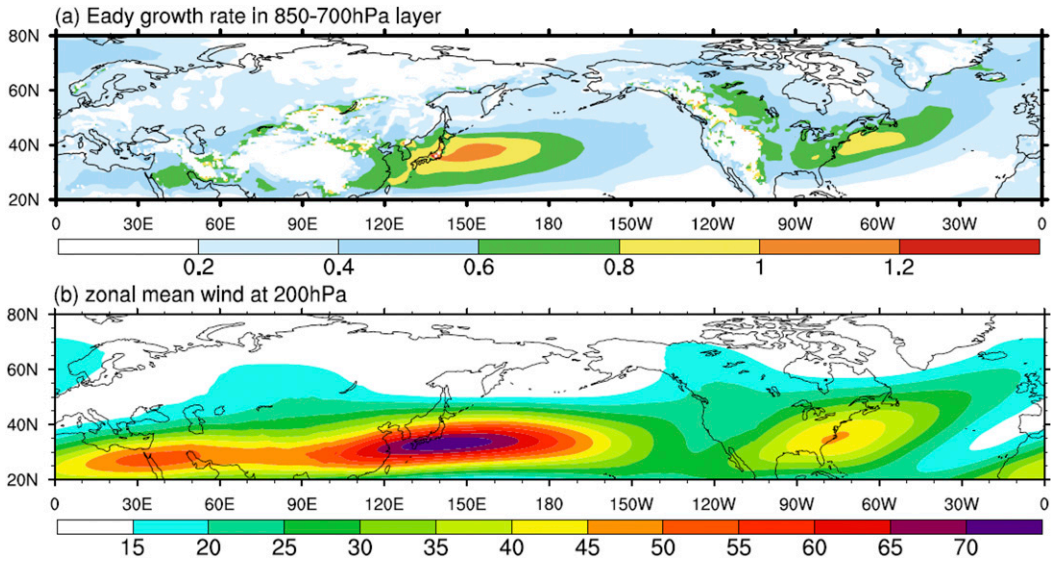

FIG. 3. (a) The 1980–2010 DJF Eady growth rate average for the 850–700-hPa layer. Values exceeding 0.2 day^{-1} are shaded at 0.2 day^{-1} intervals. Masked areas over the continents indicate regions where the land extends above the 850-hPa surface. (b) Zonal mean wind at 200 hPa. Values exceeding 15 m s^{-1} are shaded.

strong-storm-track intensity (shaded) shows an eastward shift relative to the corresponding all-storm track (contours). The substantial increase in the strength of strong Pacific storms toward the eastern ocean is indicative of their potential destructive power as they move eastward and hit the North American west coast. Unlike the Pacific track, the NAA strong-storm track retains its high intensity across its respective ocean basin. This suggests that the collocation of the low-level baroclinic zone with the highly active NAA strong-storm track helps to invigorate intense storms in the western Atlantic; in turn, the storms act to reinforce the intensity of the storm track as they propagate across the ocean.

Figures 4d,e illustrate the general temporal evolution of strong storms (shaded) that follow the storm tracks. The genesis density statistic in Fig. 4d highlights regions of cyclogenesis (i.e., the location of the strong storms' initial development). Regions of strong-storm decay are represented by the lysis density statistic (Fig. 4e). Corresponding characteristics of the all-storm tracks are also shown by contours in Figs. 4d,e to display the similarity in behavior between the all-storm and strong-storm tracks.

Strong storms that can affect North American weather tend to develop in small groups near low-level baroclinic zones westward of where the storm tracks peak in intensity (Figs. 3a and 4d). The storms propagate eastward and become strongest over the eastern North Pacific and western North Atlantic Oceans (Fig. 4c). As they continue to move eastward the strong storms tend to decay (Fig. 4e), in part as they encounter high orography and become disorganized and either dissipate or reorganize leeward of the orography and reinvigorate (Figs. 4d,e). Figure 4d also shows and supports that strong storms (e.g., intense winter nor'easter storms, which in part are influenced by heat fluxes over the Gulf Stream), tend to develop over the western North Atlantic Ocean near the northeastern United States (Kuo et al. 1991; Davis and Dolan 1993; Yao et al. 2008).

In the analysis of strong-storm tracks that influence North American weather, it is desirable to take into account the corresponding patterns of diabatic heating for the atmospheric column. Figures 5a, 5b, and 5c present the diabatic heating climatology, the heating during all storm activity, and the heating during strong-storm activity, respectively. The climatology shows positive heating rates in the western North Pacific and western North Atlantic Oceans (Fig. 5a), and this pattern resembles the low-level baroclinic instability (Fig. 3a). The distribution of positive heating rates in the Northern Hemisphere winter is influenced by the distribution of the warm Kuroshio and Gulf Stream currents in the western North Pacific and North Atlantic Oceans, respectively, and by the zonal asymmetry of the land–ocean distribution (Brown 1964; Geller and Avery 1978; Wei et al. 1983). In contrast to the climatology, the heating during all storm activity increases in strength and spreads across the North Pacific and North Atlantic Oceans in the midlatitudes (Fig. 5b). The heating is even more intense during strong-storm activity (Fig. 5c). In the North Pacific, the heating further intensifies in the east where the Pacific strong-storm

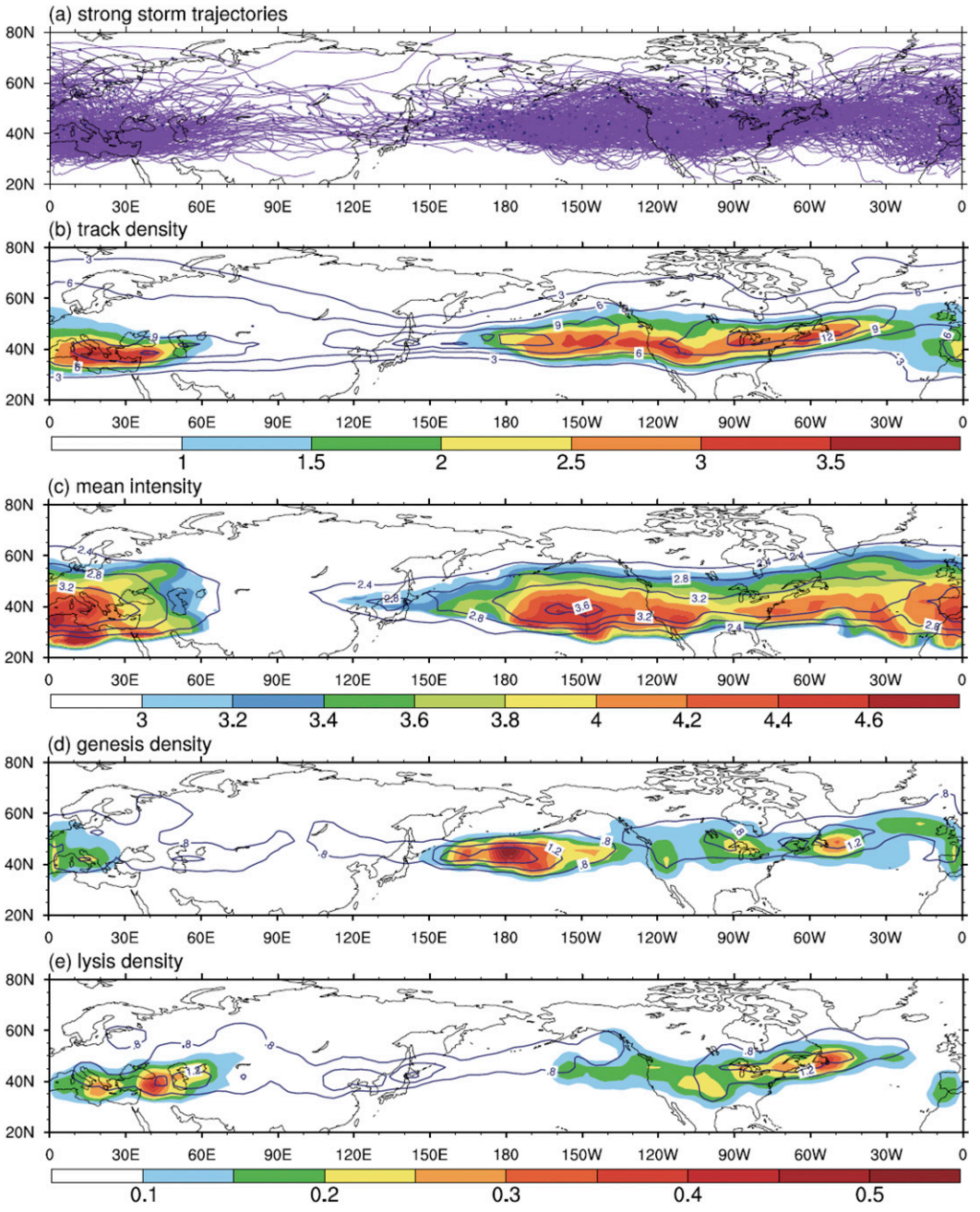

FIG. 4. Storm-track statistics in the Northern Hemisphere during DJF for 1980–2010. All-storm-track properties are depicted in contours, whereas the strong-storm-track properties are shaded. (a) Individual trajectories of strong storms. (b) Track density for all-storm tracks [contours at intervals of 3.0 storms $(10^6\,\mathrm{km}^2)^{-1}$ $(\mathrm{month})^{-1}$] and strong-storm tracks [shaded at intervals of 0.5 storms $(10^6\,\mathrm{km}^2)^{-1}$ $(\mathrm{month})^{-1}$]. (c) Mean intensity of all-storm tracks (contour intervals of 0.4 PVU) and strong-storm tracks (shaded at intervals of 0.2 PVU). (d) Cyclogenesis density for all-storm tracks [contours at intervals of 0.4 storms $(10^6\,\mathrm{km}^2)^{-1}$ $(\mathrm{month})^{-1}$] and strong-storm tracks [shaded at intervals of 0.05 storms $(10^6\,\mathrm{km}^2)^{-1}$ $(\mathrm{month})^{-1}$]. (e) As in (d), but for cyclolysis.

track is most intense, and it remains strong as it spreads up and down the west coast of North America. In relation to the NAA strong-storm track, the heating is most intense over the western North Atlantic and remains strong across the ocean where the storm track retains its high intensity.

Figure 5d presents the ratio of the positive heating rates related to strong-storm activity to the positive

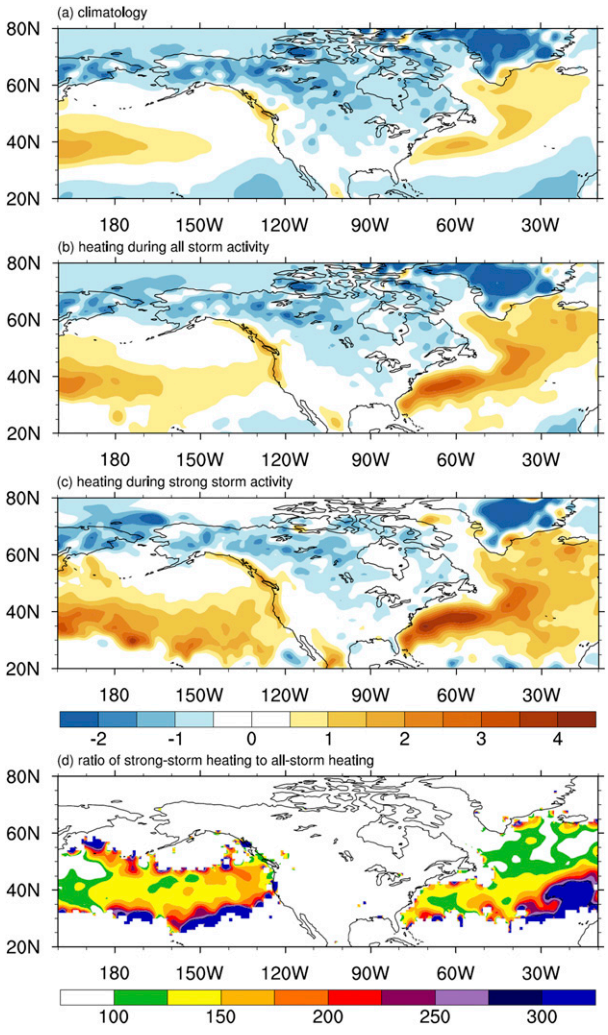

FIG. 5. DJF 1980–2010 vertically averaged 900–100-hPa diabatic heating: (a) climatology, (b) during all storm activity, and (c) during strong-storm activity. (d) The ratio (%) of the strong-storm diabatic heating to the all-storm diabatic heating. Shaded regions in (d) indicate areas where the all-storm and strong-storm heating rates are positive.

heating rates related to all storm activity. This comparison between the strong-storm and all-storm heating reveals that the heating related to the strong-storm tracks is at least 25% more intense than the heating related to the all-storm tracks over the Pacific and Atlantic Oceans where the storm tracks are strongest. Moreover, in the lower midlatitudes, the strong-storm heating is up to 3 times more intense than the all-storm heating.

Deep convection associated with strong-storm activity is obtained directly as a diagnostic from the CFSR database (Fig. 6). High positive heating rates associated with deep convection are found in each of the strong-storm-track regions and are highest where the storm

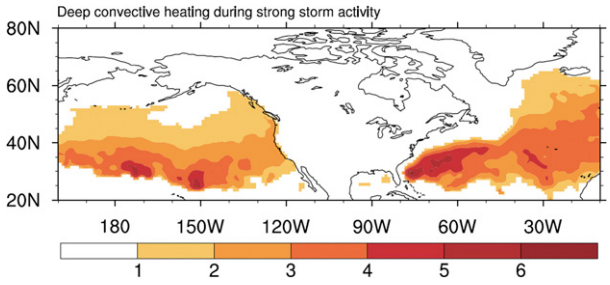

FIG. 6. Mean heating from deep convection during strong-storm activity averaged between 900 and 100 hPa in the Northern Hemisphere during DJF for 1980–2010. Contour interval is 1.0 K day^{-1}. Regions outside the all-storm-track regions are masked out.

tracks are most intense (see Figs. 4b,c). Furthermore, the heating from deep convection largely resembles the diabatic heating distribution in the strong-storm-track regions (Fig. 5c), suggesting that deep convective processes dominate the strong-storm tracks in the free atmosphere.

The strong-storm diabatic heating in the western North Atlantic corresponds with the high track density and is more intense than the heating in the North Pacific (Figs. 4b and 5c). Similar relationships are found in the deep convection associated with strong-storm tracks (Fig. 6). Along with the local SW–NE-oriented low-level baroclinic zone and upper-level jet near the east coast of North America (Fig. 3), the stronger heating in the Atlantic promotes greater instability and increased cyclonic activity (Fig. 4b), supporting the findings of Brayshaw et al. (2009).

4. Relation of storm tracks to surface weather

The near-surface wind distribution can change dramatically during the evolution of intense extratropical cyclones, and this is cause for concern for two reasons. First, in populated areas there is great potential for the wind to inflict serious damage and put lives in jeopardy, and second, over open waters strong near-surface winds have great impacts where maritime transportation, fishing vessels, and manned offshore oil and gas production units are most vulnerable (Bell et al. 2017). Strong storms can also change the winter precipitation distribution by generating excessive amounts in a relatively short amount of time (from days to a week). Lasting and possibly devastating effects like major flooding and wind damage may result leading to states of emergency, especially when the cumulative impacts and insurance losses from several storms occurring in rapid succession are considered (Mailier et al. 2006). The patterns of intense near-surface winds and heavy

precipitation rates in strong-storm tracks over North America are explored next.

a. Near-surface winds

The relation between the storm tracks and near-surface winds will be discussed next with the support of Figs. 7 and 8. In the absence of storm activity (Fig. 7a), near-surface winds achieve magnitudes of about 4–6 m s^{-1} and resemble the pattern of the upper-level jet presented in Fig. 3b with primarily eastward and northeastward directions in the North Pacific and North Atlantic Oceans, respectively. Figure 7b shows that for both the Pacific and NAA all-storm tracks (i.e., storms with $PV_{max} \geq 1$ PVU), the near-surface winds intensify where the storm tracks are strongest and shift eastward in the eastern ocean basins. The winds associated with the strong-storm tracks (i.e., $PV_{max} \geq 4.8$ PVU) presented in Fig. 7c show further intensification and a stronger eastward shift over the oceans.

The increases in wind speed related to the all-storm tracks are better seen in Figs. 8a and 8b that depict the difference and ratio, respectively, between the all-storm-related wind speeds and the no-storm wind speeds. Likewise, Figs. 8c and 8d depict the wind speed difference and ratio between strong-storm and no-storm events. In the North Pacific Ocean, wind speeds increase in the eastern basin where the all-storm track is strongest (Fig. 8a), particularly in the lower and higher midlatitudes where they are over 5 times more intense (Fig. 8b). The winds over the ocean further intensify during strong-storm activity (Figs. 8c,d), helping to drive strong storms eastward to the North American coast. Moving to the Atlantic sector, wind speeds are found to intensify across the North Atlantic but particularly in the west and lower midlatitudes with a secondary maximum toward the northeastern sector (Figs. 8a,b; also seen in Fig. 7c). During strong-storm activity, wind speeds are further enhanced, specifically in the west just offshore of North America (Figs. 8c,d). Over land, near-surface wind speeds related to the all-storm tracks increase east of the Rocky Mountains (Figs. 8a,b). Greater intensification in the wind speeds is evident during strong-storm events (Figs. 8c,d), specifically in the eastern United States where the corresponding strong-storm track strengthens (see Fig. 4c).

Overall the strong-storm tracks leave greater imprints in the near-surface wind field in the North Atlantic than in the North Pacific (Fig. 7c), most notably just offshore of North America where maritime shipping and oil platforms are exposed. Increases in wind speeds near the coasts are also more pronounced in the western North Atlantic (Figs. 8c,d), consistent with the distributions of diabatic heating and deep convection that indicate greater baroclinic instability in the region (see Figs. 5c and 6). This would suggest that maritime operations in the western North Atlantic are more at risk to damage by way of near-surface winds associated with the strong-storm tracks.

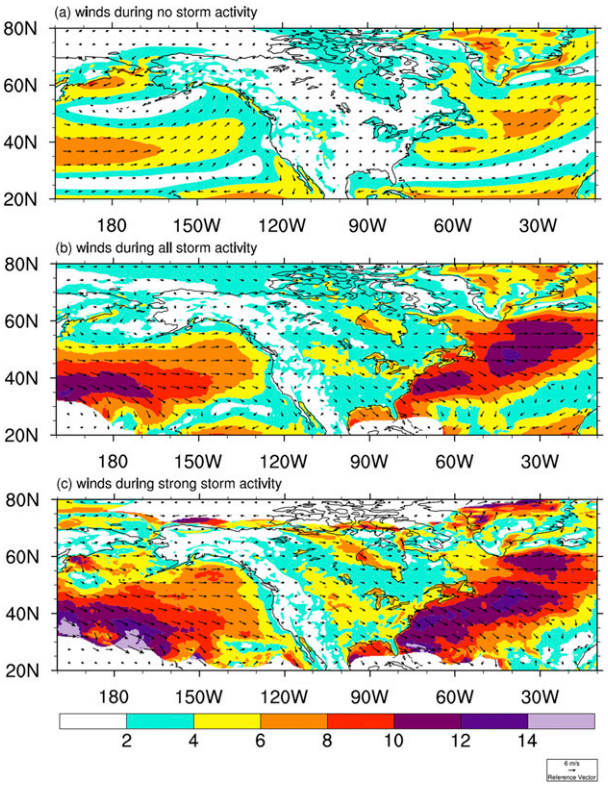

FIG. 7. Mean near-surface wind distributions on the hybrid level 1 in DJF for 1980–2010 during (a) no storm, (b) all storm, and (c) strong storm activity. Shaded intervals are 2.0 m s^{-1}. In (b) and (c), regions outside the all-storm-track regions are masked out.

The potential damage associated with extratropical strong-storm tracks over land in North America is assessed taking into account very high near-surface storm wind speeds (i.e., those that exceed the local 98th percentile; Fig. 9). Areas east of high orography experience the highest percent of strong-storm days with near-surface wind speeds above the 98th percentile (Fig. 9a). As seen in Fig. 9b, these same areas also experience the most intense wind speeds related to the strong-storm tracks.

Intense near-surface winds do not necessarily imply damage, unless they occur over populated areas. Figure 9c presents the 2010 population number obtained from the LandScan Global Population Project following the methodology in Dobson et al. (2000), which is used for the calculation of the storm loss index presented in section 2c. The storm loss estimate (Fig. 9d) highlights the regions that are most vulnerable to damage from very high

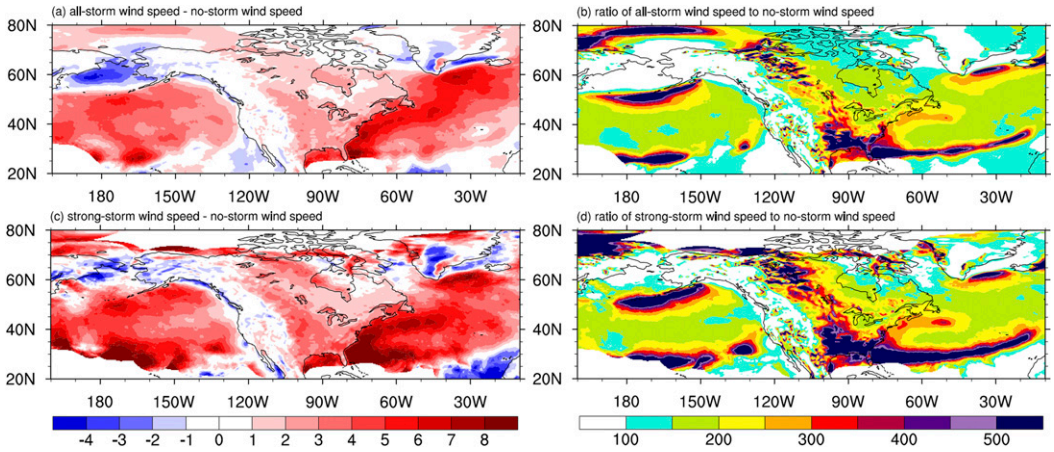

FIG. 8. Wind speed comparisons based on Fig. 7. (a) Difference between all-storm wind speed and no-storm wind speed. (b) Ratio (%) of the all-storm wind speed to the no-storm wind speed. (c) Difference between strong-storm wind speed and no-storm wind speed. (d) Ratio (%) of strong-storm wind speed to the no-storm wind speed. In (a) and (c), shaded intervals are 1.0 m s^{-1}. In (b) and (d), values exceeding 100% are shaded with intervals of 50%. Regions outside the all-storm-track regions are masked out.

storm winds. Within North America, these areas are in the eastern United States spanning from the Midwest to the U.S. East Coast states, as well as along the southwestern U.S. coast. A comparison with Fig. 9a reveals that storm wind loss in these areas is associated with up to 16% of strong storms in winter.

b. *Precipitation*

Figure 10 presents the relation between the storm tracks and surface precipitation. Figures 10a and 10b show the precipitation distributions related to all-storm tracks and to strong-storm tracks, respectively. Consistent

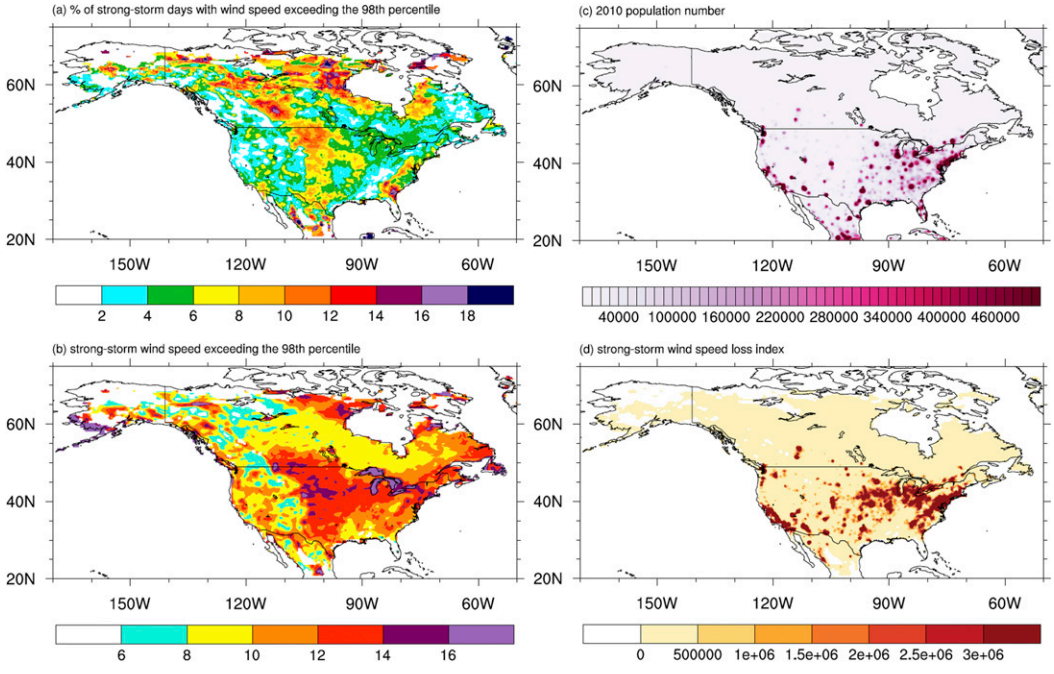

FIG. 9. Analysis of intense near-surface wind speeds in DJF for 1980–2010 in North America. (a) Percent of strong-storm days with wind speeds exceeding the local 98th percentile. Shaded intervals are 2%. (b) Mean strong-storm wind speeds exceeding the local 98th percentile. Shaded intervals are 2 m s^{-1}. (c) The 2010 population number with an interval of 10^4 people. (d) The strong-storm wind speed loss index with an interval of 5×10^5 and all positive values shaded.

with the findings in Hawcroft et al. (2012), the all-storm and strong-storm precipitation maxima are found in the North Pacific and North Atlantic Oceans as well as along the west coast of North America. Secondary precipitation maxima are found in the southeastern United States. Overall the storm tracks leave greater imprints in the precipitation in the North Atlantic than in the North Pacific, possibly associated with the warmer waters that favor increased baroclinic instability and deep convection (see Figs. 3a and 6).

The difference and ratio between the strong-storm- and all-storm-track precipitation (Figs. 10c and 10d, respectively) indicate the noticeable increases in precipitation that result from the fewer but stronger storms. These increases are evident over the oceans where the storm tracks are most intense. The percent contribution of strong-storm precipitation to the all-storm precipitation (Fig. 10e) shows that strong storms represent about 16% of all storms, yet they contribute 30%–50% of the precipitation associated with the Pacific and NAA storm tracks (discussed further below).

As expected, precipitation associated with strong-storm activity in the eastern Pacific Ocean is more intense than that associated with all storm activity (Figs. 10a–c). Toward the U.S. West Coast, precipitation increases during strong-storm activity (Figs. 10c,d) and contributes to almost half of the all-storm precipitation in the region (Fig. 10e), exposing local fishing and other maritime operations to potential damage. Further increases are found as North America's land contrasts and orographic effects come into play: in the western United States, increases of 50% are found during strong-storm activity (Figs. 10d,e). This supports the notion that cyclones aloft lead to large accumulations of precipitation upstream of great mountain ranges and other high orography (Garreaud 2007). Farther east, strong-storm tracks are also associated with more intense precipitation rates (Figs. 10c,d), contributing to over 30% of the all-storm precipitation (Fig. 10e). Orography in the northeastern United States can further boost the precipitation from strong storms. Similar results are found in the western North Atlantic where the enhanced strong-storm precipitation contributes to 30% of the all-storm precipitation (Figs. 10c–e).

The susceptibility to damage from heavy precipitation, that is, precipitation rates exceeding the local 98th percentile, during strong-storm activity is investigated for North America (Fig. 11). The percent of strong-storm days with precipitation rates exceeding the local 98th percentile is presented in Fig. 11a. Distributions of heavy precipitation related to the all-storm and strong-storm tracks are shown in Figs. 11b and 11c, respectively. The heaviest precipitation related to the all-storm

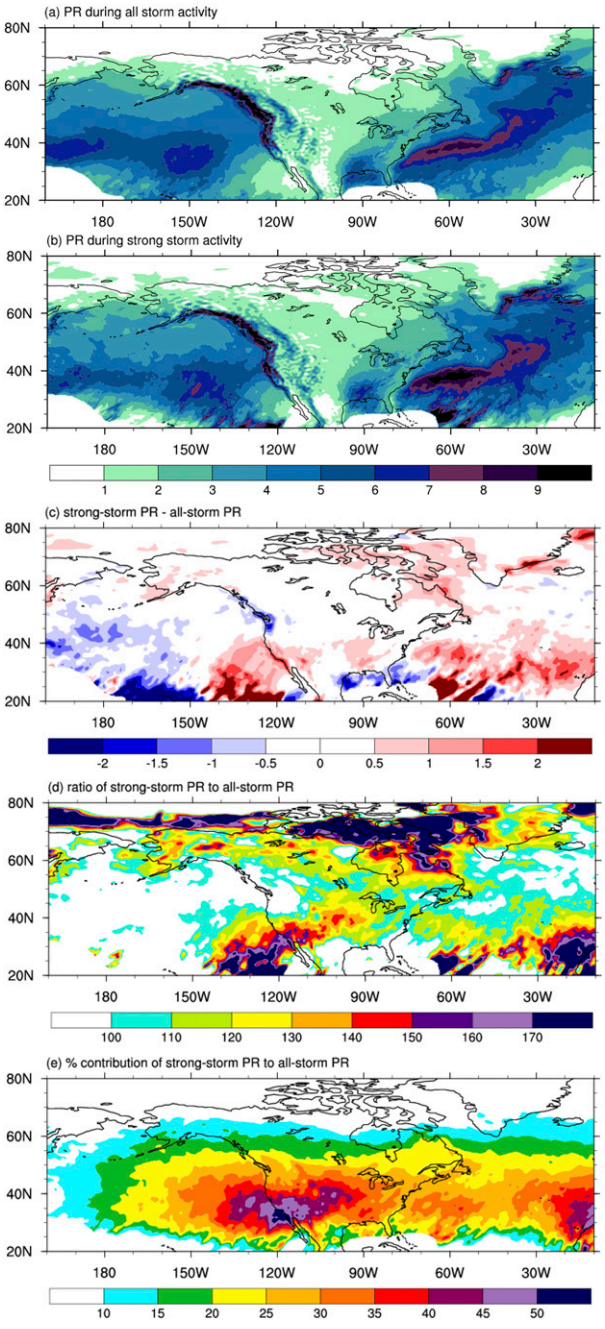

FIG. 10. Analysis of CFSR precipitation rates (PR) during DJF for 1980–2010. (a) The mean precipitation during all storm activity, and (b) the mean precipitation during strong-storm activity. In (a) and (b), shaded intervals are 1.0 mm day^{-1}. (c) The difference between strong-storm precipitation and all-storm precipitation with an interval of 0.5 mm day^{-1}. (d) The ratio (%) of strong-storm precipitation to all-storm precipitation with an interval of 10%, and values exceeding 100% are shaded. (e) Percent contribution of strong-storm to all-storm precipitation with an interval of 5%. For all panels, areas outside the all-storm-track regions are masked out.

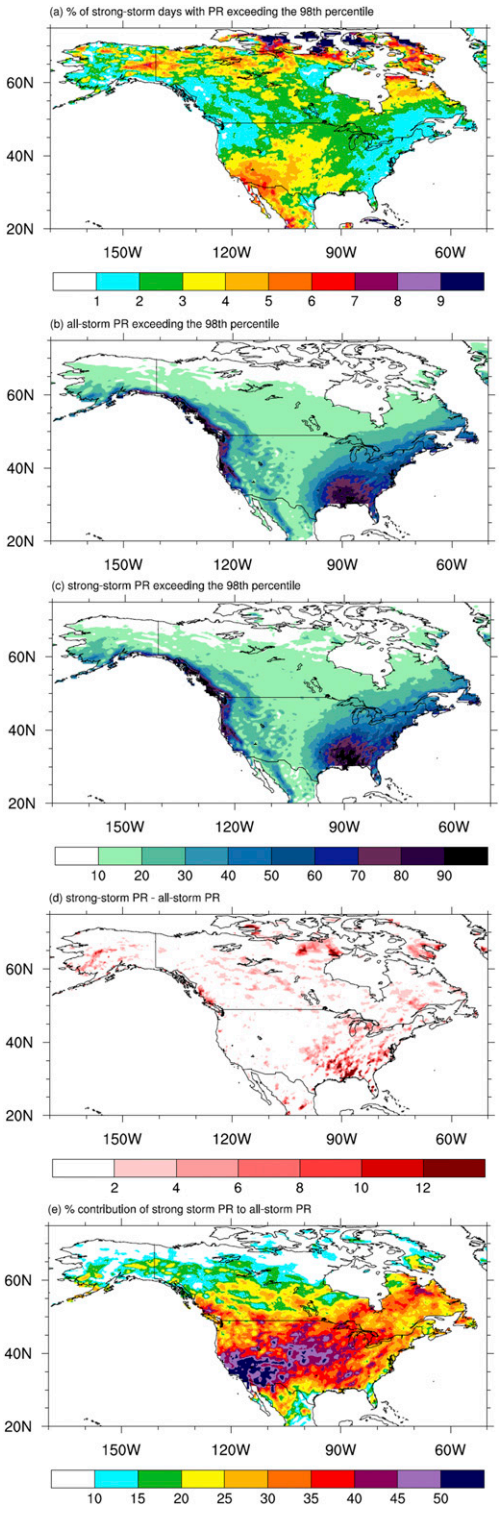

FIG. 11. Analysis of CFSR intense PR during DJF for 1980–2010 over North America. (a) The percent of strong-storm days with precipitation exceeding the local 98th percentile. Shaded intervals are 1%. (b) The all-storm precipitation that exceeds the local 98th percentile. Shaded intervals are 10 mm day^{-1}. (c) As in (b), but for strong-storm precipitation. (d) The difference between strong-storm precipitation and all-storm precipitation. Shaded intervals are 2.0 mm day^{-1}. (e) Percent contribution of strong-storm to all-storm precipitation with an interval of 5% and all values exceeding 10% shaded. Masking for all panels indicates areas where storm precipitation falls below the local 98th percentile.

and strong-storm tracks is found along the U.S. West Coast and in the southeastern United States (Figs. 11b,c). The strong-storm tracks in particular likely play key roles in shaping the precipitation distribution in the southeastern United States as the region experiences a relatively high percentage of strong-storm days with precipitation exceeding the 98th percentile (Fig. 11a). Along the West Coast where there are fewer strong-storm days with heavy precipitation, it is likely that in addition to the strong-storm tracks, other factors such as topography and land–ocean contrasts may influence the distribution of heavy precipitation. In the central United States, the high percentage of strong-storm days with heavy precipitation corresponds to low strong-storm precipitation rates (Figs. 11a,c). This indicates that in winter the region is relatively dry during strong-storm activity and is therefore less likely to experience loss associated with precipitation exceeding the 98th percentile.

Figure 11d highlights the differences between the heavy strong-storm- and all-storm-track precipitation, and Fig. 11e presents the percent contribution of strong storms to all-storm precipitation that exceeds the 98th percentile. Substantial increases in precipitation rates during strong-storm activity are found in the southeastern United States and near the U.S. East Coast (Fig. 11d). Areas with the largest increases in heavy precipitation correspond to regions where strong storms contribute well over 30% of the all-storm precipitation (Fig. 11e), indicating their vulnerability to damage related to heavy strong-storm precipitation. The southeastern United States is particularly vulnerable as precipitation is greatly enhanced during strong-storm activity and contributes almost 50% of heavy all-storm precipitation in the region.

c. *Reanalysis versus observed precipitation related to the storm tracks*

The precipitation blending algorithm in CFSR combines pentad Climate Prediction Center (CPC) Merged Analysis of Precipitation (CMAP) and daily gauge precipitation analyses of varying spatial resolutions with background 6-hourly precipitation from the Global Data Assimilation System (GDAS; Saha et al. 2010b). The blending algorithm in CFSR is latitude dependent: in the tropics it tends to the CMAP analysis, in the

midlatitudes to a gauge analysis, and in the high latitudes to the model precipitation. Therefore, despite CFSR including precipitation in its assimilation cycle, deviations from observations may occur. During 1999–2010, daily GPCP precipitation rates are considerably less intense than the daily reanalysis precipitation rates (not shown, but almost identical to the 1980–2010 reanalysis precipitation rates), particularly north of 60°N along the southern coastlines of Alaska and Greenland. As stated, this and other differences in winter precipitation between CFSR and GPCP may be caused by multiple reasons, including the precipitation blending algorithm in CFSR but also inadequate satellite-driven estimations of precipitation at high latitudes included in the daily GPCP dataset (Bolvin et al. 2009).

We examine whether the relation of the strong-storm tracks with the daily reanalysis precipitation is maintained over North America when using precipitation derived from observations, that is, the daily precipitation from GPCP (section 2). To this end, and despite that GPCP became available in 1996, the period 1999–2010 is examined to avoid any eventual spurious effects caused by the 1998 discontinuity found in CFSR. The 1999–2010 daily precipitation distributions associated with the all-storm and strong-storm tracks for GPCP are shown in Figs. 12a and 12b, respectively. Comparison with the reanalysis precipitation (Figs. 10a,b) indicates that they share similar spatial distributions with local maxima over the eastern North Pacific Ocean, the western North Atlantic Ocean, the west coast of North America, and the southeastern United States. Nevertheless, the GPCP precipitation does exhibit weaker intensities, particularly in the Pacific and NAA storm-track regions over the oceans. It is likely that the discrepancy in magnitude results from uncertainties in the oceanic observations of precipitation described in Adler et al. (2012).

Similar inferences can be noted in the difference (Fig. 12c) and ratio (Fig. 12d) of the observed precipitation related to the all-storm and strong-storm tracks. Differences in the reanalysis and observed precipitation metrics are noted particularly in the western North Atlantic Ocean where the observed precipitation related to the strong-storm tracks is shown to decrease (Fig. 12c). As already stated, the uncertainties in oceanic observations may play a role in this discrepancy. Over land, the observed precipitation differences and ratios in Figs. 12c and 12d, respectively, show increases along the U.S. West Coast and in the southeastern United States, consistent with the reanalysis (see Figs. 10c,d). The contribution of strong storms to the observed all-storm precipitation is presented in Fig. 12e. As depicted in the reanalysis (Fig. 10e), observations show that strong storms contribute over 30% of the all-storm precipitation over land and the oceans.

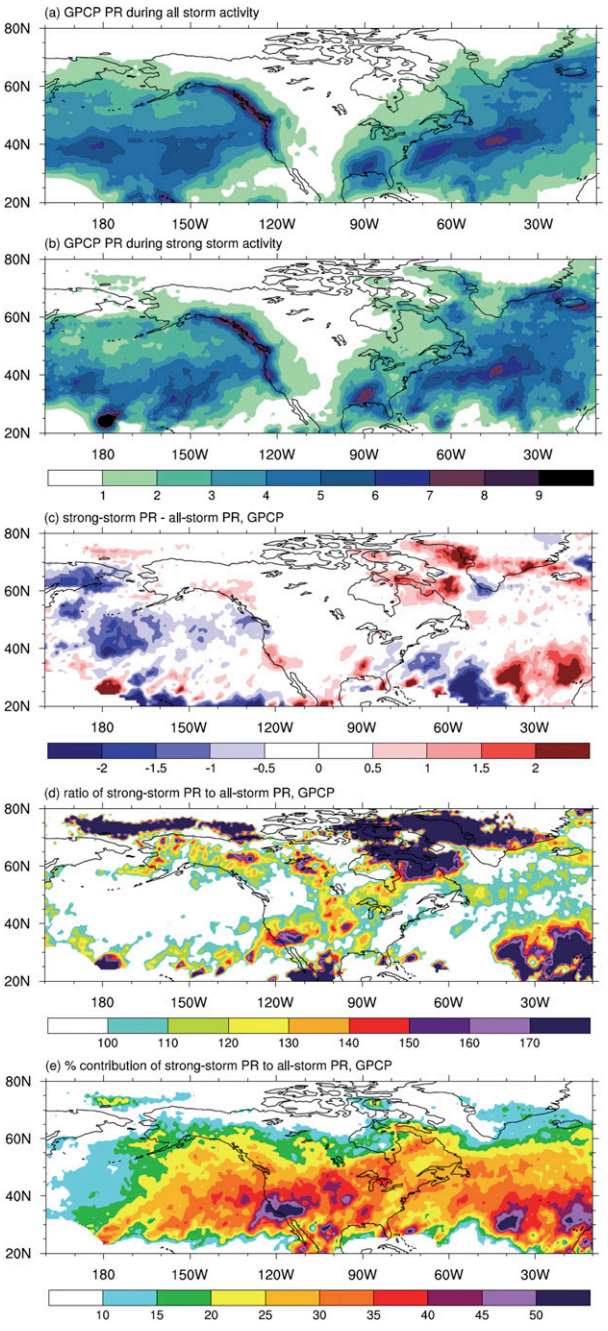

FIG. 12. As in Fig. 10, but for GPCP precipitation for 1999–2010.

We also analyze the relation of the storm tracks with precipitation from GPCP that exceeds the local 98th percentile in North America (Fig. 13). Comparison of the reanalysis (Figs. 11b–e) and observational metrics reveal similarities despite the weaker GPCP intensities. The intense precipitation observed over the continent (Figs. 13a,b) corresponds qualitatively well with the

reanalysis, in particular in the eastern United States and along the North American west coast where the precipitation is further enhanced during strong-storm activity (Fig. 13c). According to Fig. 13d, strong storms contribute over 30% of the all-storm precipitation that exceeds the 98th percentile in regions where large increases are observed. The results indicate that the eastern United States and the west coast of North America are most prone to damage from heavy strong-storm precipitation, consistent with the findings using CFSR (section 4b). In general, we find that the reanalysis precipitation distributions related to the all-storm and strong-storm tracks are consistent with observations.

d. The 1998 CFSR data discontinuity and the storm tracks

It was stated earlier that the reanalysis data show a discontinuity in the wind and precipitation fields in October 1998 thought to be due to the ingestion of data from ATOVS at the time. For instance, after 1998 there is a marked decrease in the intensity of low-level winds in the tropics and an increase in the global average precipitation (Chelliah et al. 2011; Wang et al. 2011). We investigate what impact, if any, this jump has on the results. To this end, the subset periods of 1980–98 (hereafter the early period) and 1999–2010 (hereafter the later period) are analyzed. Table 1 displays relevant strong-storm statistics for the early and later periods to assess any change in the strong winter storm tracks that could impact the North American climate. The statistics are normalized to units per season and include the number of strong storms identified, the mean intensity of the strong storms, and the average maximum intensity reached by the strong storms during each period. Furthermore, each decade between 1980 and 2010 is examined to explore the possibility of a trend in the storm tracks regardless of the discontinuity.

The more important feature noted in Table 1 (top) is that no noticeable variations are found in the statistical means between the early and later periods and among the decades within 1980–2010. This indicates that the CFSR discontinuity does not significantly influence NH storm-track behavior. Further, the effect of the discontinuity on the Pacific and NAA strong-storm tracks separately is investigated (Tables 1, middle and bottom), and it is found again that the behavior of each of the storm tracks is unaffected.

A related evaluation was performed for the relation between the strong-storm tracks and the near-surface wind and precipitation distributions (not shown). Again, it was found that the 1998 CFSR discontinuity has little or no influence on the results corresponding to North American high-impact weather. The wind speed associated with strong-storm tracks in each of these periods resembles that for the entire period and the same is true for the strong-storm precipitation. In summary, it is found that the CFSR discontinuity does not affect any of the features discussed in this article.

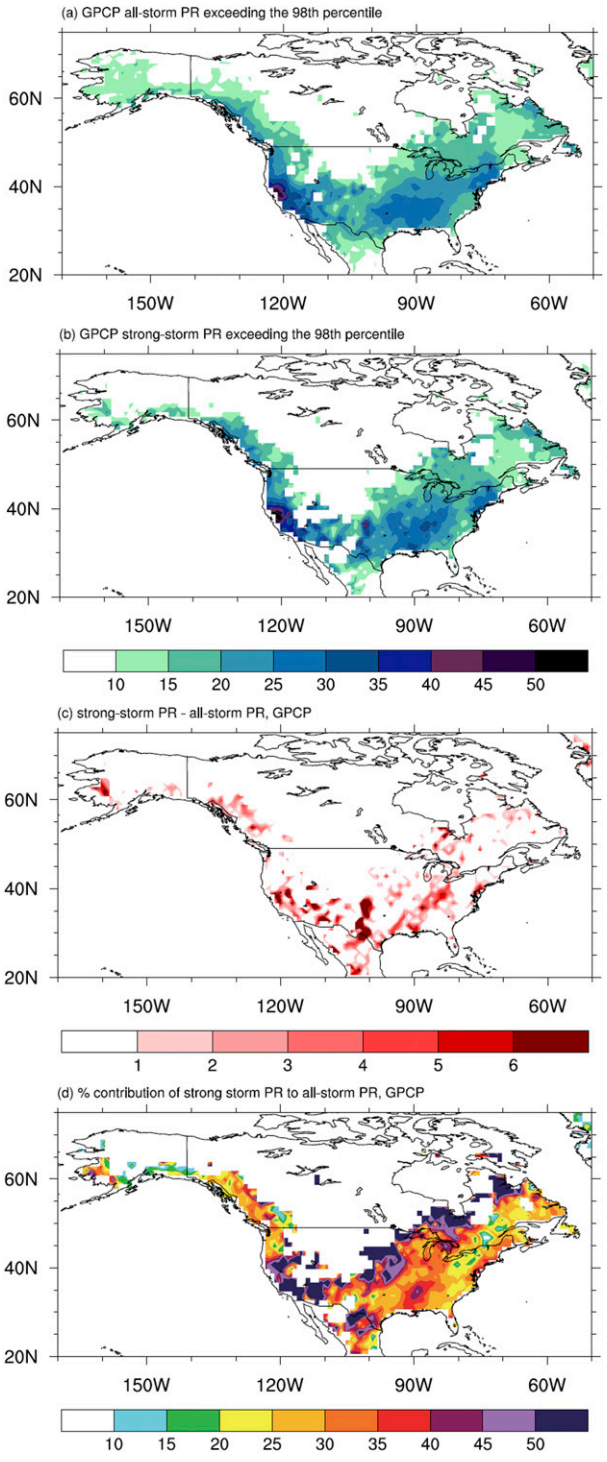

FIG. 13. As in Figs. 11b–e, but for GPCP precipitation for 1999–2010.

5. Conclusions

The behavior of strong winter storm tracks and their imprint on storm-track-related weather in North America are discussed using 31 years of data from the Climate Forecast System Reanalysis and 12 years of precipitation data from the Global Precipitation Climatology Project. It is found that a data discontinuity in October 1998 in CFSR does not affect the behavior of the Northern Hemisphere storm tracks, nor does it influence their relation with North American winter weather. Storms are defined as maxima in potential vorticity and objectively tracked through their life cycles following a Lagrangian approach. Two types of storm tracks are discussed: the first one, ''all-storm tracks,'' includes all extratropical cyclones whose maximum PV intensities exceed a low threshold of 1 PVU; the second type, ''strong-storm tracks,'' only includes storms that achieve a maximum potential vorticity of at least 4.8 PVU, which is the value exceeding the mean intensity of storms composing the Pacific and NAA storm tracks by one standard deviation. These more intense extratropical cyclones make up about 16% of all winter storms. Both all-storm tracks and strong-storm tracks are found to correspond well with those described in previous studies: over the North Pacific Ocean and over the North Atlantic Ocean (as well as a weaker one over the Mediterranean Sea). In addition to detecting larger structures like the mean intensity of the storm tracks, and because of the dependence of PV on higher-order derivatives, small-scale features of the storm tracks are easily differentiated (i.e., regions of cyclogenesis and cyclolysis). The cyclogenesis pattern shows that strong storms generally develop near low-level baroclinic zones. The cyclolysis pattern reveals that the strong storms tend to dissipate in the eastern North Pacific Ocean, the western North Atlantic Ocean near eastern Canada, and a secondary area over the central United States. The symbiotic relation between storm tracks and diabatic heating is evidenced in the large increases in diabatic heating associated with deep convective processes. The heating increases occur where the strong-storm tracks are most intense, in particular over the oceans.

The analysis of the relation of strong-storm tracks to the near-surface wind distribution indicates that the winds shift eastward during strong-storm activity. Furthermore, the wind speeds increase over the oceans where the storm tracks are most intense (i.e., in the eastern North Pacific and western North Atlantic Oceans). Over North America, areas east of the Rockies exhibit large increases in wind speed during strong-storm activity. It is found that the precipitation associated with strong-storm tracks is most intense where they are strongest. Moreover, the precipitation during strong-storm activity is more intense than that during all storm activity, especially in the North Atlantic Ocean where the NAA storm-track density is particularly high. While strong storms make up about 16% of all storms, they contribute 30%–50% of the all-storm precipitation over the oceans and over North America. Calculations based on an observed precipitation dataset (GPCP) confirm results based only on CFSR products and thus support the robustness of the findings.

The analysis of very high wind speeds and heavy precipitation related to the strong-storm tracks provides an inference of their destructive potential in North America. While the most intense strong-storm wind speeds are found in the central United States, areas most likely to experience the greatest storm wind–related loss span from the Midwest to the U.S. East Coast states as well as along the southwestern U.S. coast. Heavy precipitation is further enhanced during strong-storm activity, with the largest increases occurring along the U.S. West Coast, in the southeastern United States, and near the East Coast. In these areas, strong storms contribute over 30% of the all-storm precipitation that exceeds the local 98th percentile, indicating their vulnerability to damage from heavy precipitation during strong-storm activity.

Our findings indicate that strong-storm tracks leave a significant imprint on winter weather in North America, despite making up a small fraction of all storms that develop. This imprint depends not only on dynamical features but also on the density of the population, thus showing the greatest loss in the eastern U.S. and North American coasts. Over the water, it would be expected that oil platforms and maritime shipping and fishing craft are most vulnerable to storm-related damages just offshore of the U.S. coasts.

Acknowledgments. The authors are thankful to the anonymous reviewers for their suggestions and comments that significantly improved the article. We also acknowledge Matthew Hawcroft for computational support, and Alfredo Ruiz-Barradas, Ryan Smith, Patrick Meyers, Michael Peterson, and Stephen Doore for their helpful suggestions. This study was supported by NOAA Grant NA14NES4320003. The storm trajectories used in this study have been made freely available online in ASCII form on the Cooperative Institute for Climate and Satellites–Maryland (CICS-MD) website (http://cicsmd.umd.edu/data-downloads/data-sets/).

REFERENCES

Adler, R. F., and Coauthors, 2003: The version 2 Global Precipitation Climatology Project (GPCP) Monthly Precipitation Analysis (1979–present). *J. Hydrometeor.*, **4**, 1147–1167, https://doi.org/10.1175/1525-7541(2003)004<1147:TVGPCP>2.0.CO;2.

——, G. Gu, and G. J. Huffman, 2012: Estimating climatological bias errors for the Global Precipitation Climatology Project (GPCP). *J. Appl. Meteor. Climatol.*, **51**, 84–99, https://doi.org/10.1175/JAMC-D-11-052.1.

Barlow, M., S. Nigam, and E. H. Berbery, 1998: Evolution of the North American monsoon system. *J. Climate*, **11**, 2238–2257, https://doi.org/10.1175/1520-0442(1998)011<2238:EOTNAM>2.0.CO;2.

Bell, R. J., S. L. Gray, and O. P. Jones, 2017: North Atlantic storm driving of extreme wave heights in the North Sea. *J. Geophys. Res. Oceans*, **122**, 3253–3268, https://doi.org/10.1002/2016JC012501.

Bengtsson, L., S. Hagermann, and K. I. Hodges, 2004: Can climate trends be calculated from reanalysis data? *J. Geophys. Res.*, **109**, D11111, https://doi.org/10.1029/2004JD004536.

Berbery, E. H., and C. S. Vera, 1996: Characteristics of the Southern Hemisphere winter storm track with filtered and unfiltered data. *J. Atmos. Sci.*, **53**, 468–481, https://doi.org/10.1175/1520-0469(1996)053<0468:COTSHW>2.0.CO;2.

Bolvin, D. T., R. F. Adler, G. J. Huffman, E. J. Nelkin, and J. P. Poutiainen, 2009: Comparison of GPCP monthly and daily precipitation estimates with high-latitude gauge observations. *J. Appl. Meteor. Climatol.*, **48**, 1843–1857, https://doi.org/10.1175/2009JAMC2147.1.

Brayshaw, D. J., B. Hoskins, and M. Blackburn, 2008: The storm-track response to idealized SST perturbations in an aqua-planet GCM. *J. Atmos. Sci.*, **65**, 2842–2860, https://doi.org/10.1175/2008JAS2657.1.

——, ——, and ——, 2009: The basic ingredients of the North Atlantic storm track. Part I: Land–sea contrast and orography. *J. Atmos. Sci.*, **66**, 2539–2558, https://doi.org/10.1175/2009JAS3078.1.

Brown, J. A., Jr., 1964: A diagnostic study of tropospheric diabatic heating and the generation of available potential energy. *Tellus*, **16**, 371–388, https://doi.org/10.3402/tellusa.v16i3.8931.

Catto, J. L., C. Jakob, G. Berry, and N. Nicholls, 2012: Relating global precipitation to atmospheric fronts. *Geophys. Res. Lett.*, **39**, L10805, https://doi.org/10.1029/2012GL051736.

Chang, E. K. M., 2009: Diabatic and orographic forcing of northern winter stationary waves and storm tracks. *J. Climate*, **22**, 670–688, https://doi.org/10.1175/2008JCLI2403.1.

——, and I. Orlanski, 1993: On the dynamics of a storm track. *J. Atmos. Sci.*, **50**, 2038–2053, https://doi.org/10.1175/1520-0469(1993)050<2038:DDOBWA>2.0.CO;2.

——, S. Lee, and K. L. Swanson, 2002: Storm track dynamics. *J. Climate*, **15**, 2163–2183, https://doi.org/10.1175/1520-0442(2002)015<02163:STD>2.0.CO;2.

Chelliah, M., W. Ebisuzaki, S. Weaver, and A. Kumar, 2011: Evaluating the tropospheric variability in National Centers for Environmental Prediction's climate forecast system reanalysis. *J. Geophys. Res.*, **116**, D17107, https://doi.org/10.1029/2011JD015707.

Colucci, S. J., 1976: Winter cyclone frequencies over the eastern United States and adjacent western Atlantic. *Bull. Amer. Meteor. Soc.*, **57**, 548–553, https://doi.org/10.1175/1520-0477(1976)057<0548:WCFOTE>2.0.CO;2.

Davis, R. E., and R. Dolan, 1993: Nor'easters. *Amer. Sci.*, **81**, 428–439.

Dobson, J. E., E. A. Bright, P. R. Coleman, R. C. Durfee, and B. A. Worley, 2000: LandScan: A global population database for estimating populations at risk. *Photogramm. Eng. Remote Sens.*, **66**, 849–857.

Donat, M. G., G. C. Leckebusch, S. Wild, and U. Ulbrich, 2011: Future changes in European winter storm losses and extreme wind speeds inferred from GCM and RCM multi-model simulations. *Nat. Hazards Earth Syst. Sci.*, **11**, 1351–1370, https://doi.org/10.5194/nhess-11-1351-2011.

Garreaud, R., 2007: Precipitation and circulation covariability in the extratropics. *J. Climate*, **20**, 4789–4797, https://doi.org/10.1175/JCLI4257.1.

Geller, M. A., and S. K. Avery, 1978: Northern Hemisphere distributions of diabatic heating in the troposphere derived from general circulation data. *Mon. Wea. Rev.*, **106**, 629–636, https://doi.org/10.1175/1520-0493(1978)106<0629:NHDODH>2.0.CO;2.

Gulev, S. K., O. Zolina, and S. Grigoriev, 2001: Extratropical cyclone variability in the Northern Hemisphere winter from the NCEP/NCAR reanalysis data. *Climate Dyn.*, **17**, 795–809, https://doi.org/10.1007/s003820000145.

Hawcroft, M. K., L. C. Shaffrey, K. I. Hodges, and H. F. Dacre, 2012: How much Northern Hemisphere precipitation is associated with extratropical cyclones? *Geophys. Res. Lett.*, **39**, L24809, https://doi.org/10.1029/2012GL053866.

——, ——, ——, and ——, 2016: Can climate models represent the precipitation associated with extratropical cyclones? *Climate Dyn.*, **47**, 679–695, https://doi.org/10.1007/s00382-015-2863-z .

Held, I. M., 1993: Large-scale dynamics and global warming. *Bull. Amer. Meteor. Soc.*, **74**, 228–241, https://doi.org/10.1175/1520-0477(1993)074<0228:LSDAGW>2.0.CO;2.

Hodges, K. I., 1994: A general method for tracking analysis and its application to meteorological data. *Mon. Wea. Rev.*, **122**, 2573–2586, https://doi.org/10.1175/1520-0493(1994)122<2573:AGMFTA>2.0.CO;2.

——, 1995: Feature tracking on the unit sphere. *Mon. Wea. Rev.*, **123**, 3458–3465, https://doi.org/10.1175/1520-0493(1995)123<3458:FTOTUS>2.0.CO;2.

——, 1996: Spherical nonparametric estimators applied to the UGAMP model integration for AMIP. *Mon. Wea. Rev.*, **124**, 2914–2932, https://doi.org/10.1175/1520-0493(1996)124<2914:SNEATT>2.0.CO;2.

——, 1999: Adaptive constraints for feature tracking. *Mon. Wea. Rev.*, **127**, 1362–1373, https://doi.org/10.1175/1520-0493(1999)127<1362:ACFFT>2.0.CO;2.

——, 2008: Confidence intervals and significance tests for spherical data derived from feature tracking. *Mon. Wea. Rev.*, **136**, 1758–1777, https://doi.org/10.1175/2007MWR2299.1.

Holton, J. R., 2004: An *Introduction* to *Dynamic Meteorology*. 4th ed. International Geophysics Series, Vol. 88, Academic Press, 547 pp.

Hoskins, B. J., 1991: Towards a PV-θ view of the general circulation. *Tellus*, **43B**, 27–35, https://doi.org/10.3402/tellusb.v43i4.15396.

——, 1997: A potential vorticity view of synoptic development. *Meteor. Appl.*, **4**, 325–334, https://doi.org/10.1017/S1350482797000716.

——, and P. J. Valdes, 1990: On the existence of storm-tracks. *J. Atmos. Sci.*, **47**, 1854–1864, https://doi.org/10.1175/1520-0469(1990)047<1854:OTEOST>2.0.CO;2.

——, and K. I. Hodges, 2002: New perspectives on the Northern Hemisphere winter storm tracks. *J. Atmos. Sci.*, **59**, 1041–1061, https://doi.org/10.1175/1520-0469(2002)059<1041:NPOTNH>2.0.CO;2.

——, M. E. McIntyre, and A. W. Robertson, 1985: On the use and significance of isentropic potential vorticity maps. *Quart.*

J. Roy. Meteor. Soc., **111**, 877–946, https://doi.org/10.1002/qj.49711147002.

——, H. H. Hsu, I. N. James, M. Masutani, P. D. Sardeshmukh, and G. H. White, 1989: Diagnostics of the global atmospheric circulation based on ECMWF analyses 1979–1989. WMO/TD-326, World Meteorological Organization, 217 pp.

Hotta, D., and H. Nakamura, 2011: On the significance of the sensible heat supply from the ocean in the maintenance of the mean baroclinicity along storm tracks. *J. Climate*, **24**, 3377–3401, https://doi.org/10.1175/2010JCLI3910.1.

Huffman, G. J., R. F. Adler, M. Morrissey, D. T. Bolvin, S. Curtis, R. Joyce, B. McGavock, and J. Susskind, 2001: Global precipitation at one-degree daily resolution from multisatellite observations. *J. Hydrometeor.*, **2**, 36–50, https://doi.org/10.1175/1525-7541(2001)002<0036:GPAODD>2.0.CO;2.

——, D. T. Bolvin, and R. F. Adler, 2012: GPCP Version 1.2 1-Degree Daily (1DD) Precipitation Data Set. WDC-A, NCDC, accessed 3 June 2015, https://www.ncdc.noaa.gov/wdcmet/data-access-search-viewer-tools/global-precipitation-climatology-project-gpcp-clearinghouse.

Klawa, M., and U. Ulbrich, 2003: A model for the estimation of storm losses and the identification of severe winter storms in Germany. *Nat. Hazards Earth Syst. Sci.*, **3**, 725–732, https://doi.org/10.5194/nhess-3-725-2003.

Kuo, Y.-H., R. J. Reed, and S. Low-Nam, 1991: Effects of surface energy fluxes during the early development and rapid intensification states of seven explosive cyclones in the western Atlantic. *Mon. Wea. Rev.*, **119**, 457–476, https://doi.org/10.1175/1520-0493(1991)119<0457:EOSEFD>2.0.CO;2.

Lindzen, R. S., and B. Farrell, 1980: A simple approximate result for maximum growth rate of baroclinic instabilities. *J. Atmos. Sci.*, **37**, 1648–1654, https://doi.org/10.1175/1520-0469(1980)037<1648:ASARFT>2.0.CO;2.

Ma, C.-G., and E. K. M. Chang, 2017: Impacts of storm-track variations on wintertime extreme weather events over the continental United States. *J. Climate*, **30**, 4601–4624, https://doi.org/10.1175/JCLI-D-16-0560.1.

Maddox, R. A., C. F. Chappell, and L. R. Hoxit, 1979: Synoptic and meso-scale aspects of flash flood events. *Bull. Amer. Meteor. Soc.*, **60**, 115–123, https://doi.org/10.1175/1520-0477-60.2.115.

Mailier, P. J., D. B. Stephenson, C. A. T. Ferro, and K. I. Hodges, 2006: Serial clustering of extratropical cyclones. *Mon. Wea. Rev.*, **134**, 2224–2240, https://doi.org/10.1175/MWR3160.1.

Mak, M., 1998: Influence of surface sensible heat flux on incipient marine cyclogenesis. *J. Atmos. Sci.*, **55**, 820–834, https://doi.org/10.1175/1520-0469(1998)055<0820:IOSSHF>2.0.CO;2.

Minobe, S., A. Kuwano-Yoshida, N. Komori, S.-P. Xie, and R. J. Small, 2008: Influence of the Gulf Stream on the troposphere. *Nature*, **452**, 206–209, https://doi.org/10.1038/nature06690.

——, M. Miyashita, A. Kuwano-Yoshida, H. Tokinaga, and S.- P. Xie, 2010: Atmospheric response to the Gulf Stream: Seasonal variations. *J. Climate*, **23**, 3699–3719, https://doi.org/10.1175/2010JCLI3359.1.

Orlanski, I., and E. K. M. Chang, 1993: Ageostrophic geopotential fluxes in downstream and upstream development of baroclinic waves. *J. Atmos. Sci.*, **50**, 212–225, https://doi.org/10.1175/1520-0469(1993)050<0212:AGFIDA>2.0.CO;2.

Pendergrass, A., and Coauthors, 2015: The Climate Data Guide: GPCP (Daily): Global Precipitation Climatology Project. UCAR/NCAR, accessed 3 June 2015, https://climatedataguide.ucar.edu/climate-data/gpcp-daily-global-precipitation-climatology-project.

Pfahl, S., and H. Wernli, 2012: Quantifying the relevance of cyclones for precipitation extremes. *J. Climate*, **25**, 6770–6780, https://doi.org/10.1175/JCLI-D-11-00705.1.

Raible, C. C., 2007: On the relation between extremes of midlatitude cyclones and the atmospheric circulation using ERA40. *Geophys. Res. Lett.*, **34**, L07703, https://doi.org/10.1029/2006GL029084.

Saha, S., and Coauthors, 2010a: NCEP Climate Forecast System Reanalysis (CFSR) 6-hourly products, January 1979 to December 2010. NCAR Computational and Information Systems Laboratory Research Data Archive, accessed 11 March 2014, https://doi.org/10.5065/D69K487J.

——, and Coauthors, 2010b: The NCEP Climate Forecast System Reanalysis. *Bull. Amer. Meteor. Soc.*, **91**, 1015–1057, https://doi.org/10.1175/2010BAMS3001.1.

Salathé, E. P., Jr., 2006: Influences of a shift in North Pacific storm tracks on western North American precipitation under global warming. *Geophys. Res. Lett.*, **33**, L19820, https://doi.org/10.1029/2006GL026882.

Simmons, A. J., and B. J. Hoskins, 1979: The downstream and upstream development of unstable baroclinic waves. *J. Atmos. Sci.*, **36**, 1239–1254, https://doi.org/10.1175/1520-0469(1979)036<1239:TDAUDO>2.0.CO;2.

Sinclair, M. R., 1997: Objective identification of cyclones and their circulation intensity, and climatology. *Wea. Forecasting*, **12**, 595–612, https://doi.org/10.1175/1520-0434(1997)012<0595:OIOCAT>2.0.CO;2.

Trenberth, K. E., A. Dai, R. M. Rasmussen, and D. B. Parsons, 2003: The changing character of precipitation. *Bull. Amer. Meteor. Soc.*, **84**, 1205–1217, https://doi.org/10.1175/BAMS-84-9-1205.

Wallace, J. M., G.-H. Lim, and M. L. Blackmon, 1988: Relationship between cyclone tracks, anticyclone tracks, and baroclinic waveguides. *J. Atmos. Sci.*, **45**, 439–462, https://doi.org/10.1175/1520-0469(1988)045<0439:RBCTAT>2.0.CO;2.

Wang, W., P. Xie, S. H. Yoo, Y. Xue, A. Kumar, and X. Wu, 2011: An assessment of the surface climate in the NCEP climate forecast system reanalysis. *Climate Dyn.*, **37**, 1601–1620, https://doi.org/10.1007/s00382-010-0935-7.

Wei, M.-Y., D. R. Johnson, and R. D. Townsend, 1983: Seasonal distributions of diabatic heating during the First GARP Global Experiment. *Tellus*, **35A**, 241–255, https://doi.org/10.1111/j.1600-0870.1983.tb00201.x.

Xie, P., R. Joyce, S. Wu, S. Yoo, Y. Yarosh, F. Sun, and R. Lin, 2017: Reprocessed, bias-corrected CMORPH global high-resolution precipitation estimates from 1998. *J. Hydrometeor.*, **18**, 1617–1641, https://doi.org/10.1175/JHM-D-16-0168.1.

Yao, Y., W. Perrie, W. Zhang, and J. Jiang, 2008: Characteristics of atmosphere-ocean interactions along North Atlantic extratropical storm tracks. *J. Geophys. Res.*, **113**, D14124, https://doi.org/10.1029/2007JD008854.

Zhang, L., A. Kumar, and W. Wang, 2012: Influence of changes in observations on precipitation: A case study for the Climate Forecast System Reanalysis (CFSR). *J. Geophys. Res.*, **117**, D08105, https://doi.org/10.1029/2011JD017347.